An experimental investigation of evanescent wave propagation through a turning depth

Allison Lee and Julie Crockett

Brigham Young University
allisonlee8@byu.edu

Abstract

The formation of internal waves from evanescent regions is studied experimentally with a Gaussian topography and varying natural frequency (N) profiles. When a topography is encompassed by an evanescent region, where N is less than the imposed excitation frequency, only evanescent waves are generated. The amplitude of these evanescent waves decay at an exponential rate while traveling vertically. An evanescent wave can become a propagating internal wave when it passes through a turning depth where N is equivalent to the excitation frequency. Two-dimensional experiments are performed with exponentially varying stratifications to investigate energy transmitted from an evanescent wave to a propagating internal wave. These experiments focus on how internal wave energy is influenced by the location of the topography relative to the turning depth and the ratio of natural frequency near the topography to the excitation frequency. Internal wave energy is estimated from the experiments using Synthetic Schlieren and compared to linear theory.

1 Introduction

Internal waves play a critical role in understanding oceanic and atmospheric dynamics. In the ocean, these waves propagate away from their generation sites and can transmit energy upward from the ocean floor when generated over topography, or downward from the ocean surface when generated by strong winds at the surface. When internal waves eventually steepen and break, mixing is induced which helps to maintain healthy oceans and can affect both weather and climate patterns in the atmosphere [Lighthill (1974), St. Laurent and Garrett (2002), Nappo (2002), Sutherland (2010)].

Internal waves are formed in stratified fluids where the natural frequency (N) is less than an excitation frequency. The natural frequency is defined as

$$N^2 = (-g/\rho_o)(d\rho/dz) \tag{1}$$

where g is the gravity constant, ρ_o is a reference density and $d\rho/dz$ is the change in density with respect to height where z is positive upward. When an excitation frequency is greater than N, the bulk fluid cannot respond to the disturbance and evanescent waves are formed. Evanescent wave energy is transported vertically, and the amplitude of these waves decay at an exponential rate. Evanescent waves are often considered to have little impact on the surrounding fluid because of their large amplitude decay rate [Lighthill (1974), Pedlosky (2003)]. However, when the excitation frequency is less than the natural frequency ($\omega < N$), propagating internal waves are generated. These waves propagate away from their generation sites at an angle α away from the vertical, where $\omega = N\cos(\alpha)$. There is little to no attenuation of the amplitude of internal waves in a constant stratification. Linear theory indicates that if an evanescent wave travels vertically and reaches a depth where $\omega = N$, and thereafter $\omega < N$, then the evanescent wave can become a propagating internal wave [Nappo (2002)]. The location where $\omega = N$ is the turning depth. The M_2

lunar semi-diurnal tide oscillates above topography within the ocean and is a well known generator of internal waves, but King et al. (2012) found that there are multiple locations in the ocean where the natural frequency falls below the M_2 tidal frequency (ω_{M2} = 1.4052 x 10^{-4} rad/s). Thus there are a significant number of turning depths within the ocean, with topography which would generate only evanescent waves from the M_2 tide. Numerical simulations performed by Paoletti et al. (2014) found that the wave power transferred from an evanescent region to a propagating region was very weak relative to that of an internal wave formed over topography completely within a propagating region. However, there could still be significant energy transferred from the evanescent regions to propagating regions, depending on how close the topography is to the turning depth and the relative strength of the stratification. Using exponential stratifications, as is frequently seen in the deep ocean [King et al. (2012)], we perform an experimental investigation of both of these effects to understand the impact of evanescent regions and compare experimental results to linear theory.

2 Methods

2.1 Experimental Setup

Experiments were performed in an acrylic tank measuring 2.45m x 0.15m x 0.91m (length x width x height). Each stratification was created using a variation of the double bucket method [Hill (2002)] with N varying between 0.8-2.0s^{-1} for each test. The density profiles were chosen to reflect the exponential oceanic profiles found by King et al. (2012) and were set to the form

$$\rho = ae^{bz} + c \tag{2}$$

Values for the coefficients of a, b, and c for each case, along with the corresponding values of N_{min} and N_{max}, are shown in Table 1. A Gaussian shaped topography was oscillated at a constant frequency, though the frequencies varied between 1.0 and 1.3 s^{-1} for each case and were chosen based on the density profile. Case specific frequencies are also defined in Table 1. All of the experiments used the same Gaussian topography, which was 30 cm long, 9 cm wide, and 10 cm tall at the peak. The topography shape is described by H = $10exp(-x^2/2\sigma^2)$ with -15cm $< x <$ 15cm and $\sigma = 3$. Tests were recorded using a jAi Cv-M4+Cl progressive scan camera running at 6 fps. The topography was set to run for 15 periods before recording began to allow the system to reach steady state. Each test lasted three minutes. Synthetic Schlieren was used to capture the wave motion and each test was processed using Digiflow to calculate changes in the natural frequency (ΔN^2) [Dalziel et al. (2000)].

Kinetic energy was estimated using two separate sets of equations. The first set of equations is based off the work of Wunsch and Brandt (2012), who used planar wave velocities multiplied by an amplitude which varied slowly in the z direction. They related internal wave velocities and ΔN^2 to form the equation

$$KE_{prop} = \frac{\omega^2 N^2}{k^2(N^2 - \omega^2) + (\omega \partial_z N^2/N^2)} \left| \frac{\Delta N_o^2}{N^2} \right|^2 \tag{3}$$

Here ΔN_o^2 represents the Fourier coefficients of ΔN^2 and k is the horizontal wavenumber. This equation however is not valid in the evanescent region. Instead, the following equations define wave propagation.

$$u = Ue^{-qz}e^{-i(kx-\omega t)} \tag{4}$$

$$w = We^{-qz}e^{-i(kx-\omega t)} \tag{5}$$

$$\Delta N^2 = \Delta N_o^2 e^{-qz}e^{-i(kx-\omega t)} \tag{6}$$

$$q^2(z) = k^2(1 - N^2(z)/\omega^2) \tag{7}$$

Following the methods outlined by Wunsch and Brandt to derive (3), we find

$$KE_{evan} = \left|\frac{q\omega\Delta N_o^2}{k(\omega\partial_z N^2 + qN^2)}\right|^2 + \left|\frac{i\omega\Delta N_o^2}{\omega\partial_z N^2 + qN^2}\right|^2 \tag{8}$$

It should be noted that $m_1 = iq$, which accounts for the decaying wave. Thus while q is real and is used throughout this paper, the vertical wavenumber in the evanescent region, m_1, is imaginary.

Each test provided a window of 1360x1030 pixels, with 1080 time steps. Figure 1a is a standard image created with Digiflow where the magnitudes of ΔN^2 are shown. The topography is in the top left corner and a depiction of it has been superimposed over this image. The height of the topography, H, the distance from the tip of the topography to the turning depth, D, and the height of the turning depth, Hr, are also shown. Table 1 includes H/D for each case. Note how the evanescent wave moves vertically downward towards the turning depth, and then the internal wave starts at the turning depth and propagates away along a curve. This curve is due to the exponential density profile. For each experiment, the exact location of the wave varied depending on the horizontal location of the camera. To analyze each case, a horizontal line of data was taken through time at specific pixel heights. The starting point of each horizontal line was chosen to match a curve fit of the wave in order to capture the actual wave. Figure 1b represents the entire experimental window and includes both the curve fit of the wave from Figure 1a and the corresponding horizontal lines used for analysis. The data lines were taken at every tenth pixel along the height of the window, but the horizontal starting point varied depending on the region of the data. The horizontal starting points in the propagating region were determined by the curve fit to maximize the amount of relevant data. Notice that to the left of the curve in Figure 1a there is little to no information. In other cases, the topography was more centered and the left leg of the internal wave beam is visible. To maintain similarity between cases, only the right half of the internal wave beam was analyzed. For the evanescent region, the horizontal starting location was the same for each data line because the evanescent wave travels vertically downward and does not curve.

Table 1: The experimental setup of the 5 separate tests performed. The coefficients a, b, and c correspond to Equation 2. See Figure 1a for the locations of H and D within the experiment window.

Case	$\boldsymbol{a}$	$\boldsymbol{b}$	$\boldsymbol{c}$	$\boldsymbol{N_{min}}$	$\boldsymbol{N_{max}}$	$\boldsymbol{\omega}$	**H/D**
1a 1b	147.12	-1.73	969.46	0.9618	1.580	1.282	0.431
2a 2b	143.39	-1.71	969.31	0.9365	1.551	1.083	1.70
3a 3b	151	-2.5	986.01	0.8964	1.9252	1.168	0.903
4	158.53	-2.14	974.07	0.947	1.8227	1.083	2.94
5	158.53	-2.14	974.07	0.947	1.8227	1.083	1.786

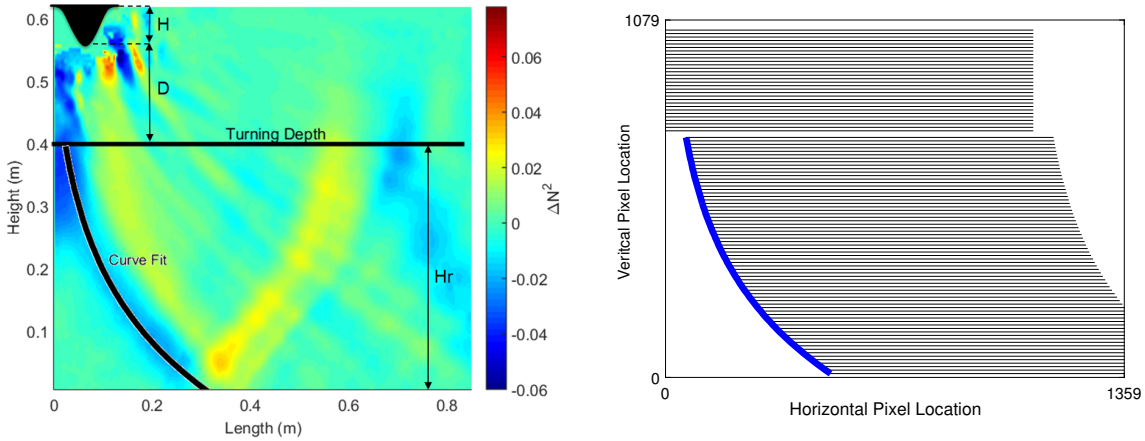

(a) Digiflow Results

(b) Horizontal line locations

Figure 1: In (a), standard Digiflow results are shown for Case 3b along with the turning depth, the curve fit of an internal wave in the propagating region, and important length scales. Image (b) has the same curve fit and includes the horizontal lines used for analysis plotted against the curve for the propagating region. The evanescent region is visible in the upper portion of the experiment window.

A two-dimensional Fourier transform was performed on the individual horizontal lines of data through time. The Fourier amplitudes were then used in (3) or (8), along with the corresponding N value for the height, to estimate the kinetic energy. The reported energy values come from summing the energy of frequencies near the excitation frequency, as this location and the frequencies directly around it always contained the highest energy.

2.2 Linear Theory

A linear analysis of wave propagation from an evanescent to a propagating region was also completed. This method is similar to that performed by Pedlosky (2003). To match the domain of the experiments, the height of the computational domain was chosen from $0< z <$0.6m, with the propagating region from $z = 0$ to $z =$ Hr and the evanescent region from $z =$ Hr to $z =$ 0.6m.

Following Pedlosky (2003) for a slowly varying wave, the vertical velocity in the propagating region was defined as

$$w_2 = A_2 e^{i(kx-\omega t+\theta_2)} \tag{9}$$

$$A_2(z) = A_{2o}/(m/m_o)^{1/2} \tag{10}$$

$$\theta_2 = \int_{z_o}^{z} m dz \tag{11}$$

$$m = k\left[N^2/\omega^2 - 1\right] \tag{12}$$

The amplitude A_2 varies with height due to the change in both N and the vertical wavenumber, m, with height. Pedlosky (2003) notes that θ_2 would become mz for a purely planar wave, however the integration is necessary due to the varying stratification. Equations 9 through 11 assume that both A_2 and θ are slowly varying functions of z. The value for A_{2o} was calculated from experimental results using the kinetic energy at a height of 0.2m, along with the associated N and m values at this height. This location

was chosen because it is far from the turning depth and the bottom boundary for all cases shown. Using continuity, the horizontal velocity was defined by

$$u_2 = \frac{-w_2}{k}\left[\frac{-dm/dz}{2im} + m\right] \tag{13}$$

Kinetic energy in the propagating region is calculated per unit volume using

$$KE = u^2 + w^2 \tag{14}$$

We defined the vertical velocity in the evanescent region in a similar manner to the propagating region but also allow the vertical component to decay. The vertical wavenumber is defined by q (see (7)), and A_1 and θ_1 were again assumed to be slowly varying functions of z. Using continuity u_1 can be found.

$$w_1 = A_1 e^{i(kx-\omega t)} e^{\theta_1} \tag{15}$$

$$u_1 = \frac{-w_1}{ik}\left[\frac{-dq/dz}{2q} + q\right] \tag{16}$$

$$A_1(z) = A_{1o}/(q/q_o)^{1/2} \tag{17}$$

$$\theta_1 = \int_{z_o}^{z} q dz \tag{18}$$

Kinetic energy was then calculated using Equation 14. In both regions, as the wave approaches the turning depth the amplitudes approach infinity. In order to circumvent this difficulty and relate each region to the experimental data, we chose to calculate A_1 from the experimental kinetic energy analysis of the evanescent region. A_{1o} was chosen at a depth of 0.5m as this location is centrally located between the topography and the turning depth for each experiment. In the future, a matching boundary condition at the turning depth will be used to relate A_1 and A_2.

3 Results

Kinetic energy as a function of height is shown for a representative case, 2b, in Figure 2a. Each point corresponds to the lines in Figure 1b. Starting at the top of the image, the kinetic energy decreases rapidly as the evanescent wave travels vertically down towards the turning depth. Beyond the turning depth, the evanescent wave has become an internal wave. Oscillations in the kinetic energy are clearly visible, along with a slight decay in the oscillation amplitude. It is possible that the oscillation is due to a lack of resolution in the lower half of the experimental window. Comparing the experiment to the linear model, a similar oscillation and slight decay is seen. This is reasonable for the linear model as θ_2 would create oscillations and the decay of A_2 would cause a decay in the overall kinetic energy. Further investigation of the oscillation and decay in the experiment would require an increased spatial resolution and then a more accurate comparison between the linear model and experimental values could be made. For the evanescent region, the linear model shows a sharp decrease in the energy, followed by a slight increase. This compares well with the experiments. While each of the models have been matched to specific locations in the experimental results, the overall behavior of both models provides insight to the experiments performed. It is expected that the evanescent model with varying N can be

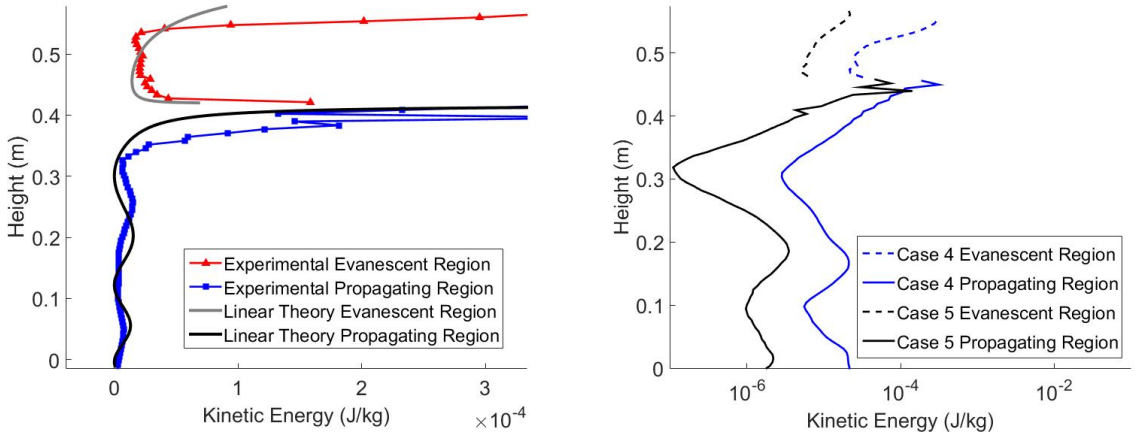

(a) Case 2b Results

(b) Case 4 and 5 Results

Figure 2: Results from two separate tests are shown. In (a), comparison of the experimetnal and linear theory results is shown for case 2b. In (b) the experimental results of case 4 and 5 are compared.

used in conjunction with the previously defined propagating model [Pedlosky (2003)] to match the behavior between the two regions.

To explore the effects of H/D, cases 4 and 5 are compared. Both tests were performed at the same excitation frequency and within the same density profile, but for case 4 the topography was situated closer to the turning depth. The ratio of H/D for case 4 was 2.94, while case 5 was 1.79. The kinetic energy for both experiments is plotted in Figure 2b. It can be seen that case 4 has an overall higher energy content than case 5. These results show clearly that evanescent wave energy decays exponentially, and the effects of that decay are visible in the propagating region as the internal wave in case 4 maintains a higher energy content than case 5 throughout the height. The difference in energy is due to the evanescent waves in case 5 traveling farther before reaching the turning depth, causing the wave to decay over a greater distance compared to the waves in case 4. The two experiments share the same phase and general shape, leading to the conclusion that the overall effect of topography location relative to the turning depth is seen in the energy content of the wave. The same trend was seen in comparing the models of the two cases.

A summary of the results for each case is listed in Table 2. The Froude numbers shown are calculated as $Fr_{evan} = \omega/N_{min}$ and $Fr_{prop} = \omega/N_{max}$. The energy input to the experiment was estimated as $\mathrm{KE}_{input} = u^2_{ave,top}$, where $u_{ave,top}$ is the average velocity of the topography. This does not account for dissipation of energy due to friction of the topography sliding on the track, or losses due to any generated turbulence, but is instead only a first order approximation of input energy. The output kinetic energy of each region was normalized by the input energy, and these ratios are shown in Table 2. The output energy for the evanescent region is taken as the minimum kinetic energy in that region, while the output for the propagating region is the average kinetic energy of the oscillating portion of the region. Values near the turning depth were not included for either region. Cases 1-3 each had two runs, so the normalized energy was averaged between the runs. In the evanescent region, the model consistently under-predicts the kinetic energy compared to the experimental results. The reverse is true in the propagating region where the model over-predicts the kinetic energy. Comparing the experimental results, the minimum kinetic energy in the evanescent region is always greater than the average energy in the

propagating region, as would be expected. Further comparisons of the linear models will be made once the models have been matched.

Table 2 shows that increasing H/D will increase the total energy in both the evanescent and the propagating regions. As a large value for H/D indicates that the topography is near the turning depth, this is a reasonable result. Comparing case 1 and 3, values for Fr_{evan} and Fr_{prop} are very similar. The main difference between the cases comes from H/D, which is almost doubled from case 1 to case 3. The energy in case 3 is a little over 30 times that of case 2. Cases 4 and 5 also have similar increases in H/D, though H/D is larger and the normalized energy of the propagating region for case 4 is not quite triple that of case 5. This could indicate a trend that while increasing H/D does increase the kinetic energy in the propagating region, the effect diminishes for large values of H/D.

Another trend seen in Table 2 is that increasing Fr_{evan} and Fr_{prop} leads to a decrease in kinetic energy. Increasing Fr_{evan} indicates that the natural frequency near the topography is decreasing. A weak stratification would generate waves with low kinetic energy, and that energy would die away more rapidly as the wave traveled to the turning depth. It is possible that increasing Fr_{evan} would dominate over the effects of Fr_{prop} on kinetic energy as the evanescent wave amplitudes are expected to decay exponentially, whereas there is only a slight decay in the propagating region. The only significant variation in energy and Fr_{prop} is seen in case 1 and 3, but these cases also have large changes in H/D. Case 3 also shows a very similar relative energy between the experimental evanescent and propagating regions, but the same trend is not seen in case 1, where Fr_{prop} is greater than case 3, lending to the idea that increasing Fr_{prop} will decreases the kinetic energy in the propagating region. Further exploration of the independent effects of Fr_{evan} and Fr_{prop} are needed before more conclusions can be drawn.

Table 2: A summary of the results for each case is presented.

Case	$\boldsymbol{Fr_{evan}}$	$\boldsymbol{Fr_{prop}}$	**H/D**	**Normalized Energy Evanescent Region**		**Normalized Energy Propagating Region**	
				$\mathbf{KE_{evan,exp}}$	$\mathbf{KE_{evan,model}}$	$\mathbf{KE_{prop,exp}}$	$\mathbf{KE_{prop,model}}$
1a 1b	1.33	0.817	0.431	0.0063± 0.0003	0.0003 ± 0.0001	0.0010 ± 0.0001	0.0019 ± 0.0003
2a 2b	1.15	0.698	1.70	0.116 ± 0.03	0.0861 ± 0.010	0.0439 ± 0.012	0.0651 ± 0.04
3a 3b	1.30	0.607	0.903	0.0342 ± 0.006	0.0198 ± 0.005	0.0301 ± 0.0008	0.0514 ± 0.0017
4	1.14	0.594	2.94	0.135	0.160	0.0643	0.125
5	1.14	0.594	1.79	0.081	0.101	0.0248	0.0804

4 Conclusion

An investigation of energy transfer from evanescent to propagating regions was performed. By expanding on the experimental equations of Wunsch and Brandt (2012) and linear model of Pedlosky (2003), equations and models to estimate kinetic energy within evanescent regions were derived. An analysis of the kinetic energy results showed that increasing H/D can lead to sharp increases of kinetic energy transferred from evanescent regions to propagating regions. The opposite is true for increasing Fr_{evan} and Fr_{prop}, as relative kinetic energy decreased with increasing Fr. Future work will combine the linear models by matching boundary conditions at or near the turning depth to further explore

the effects of Fr and H/D. These results will be extrapolated to calculate oceanic energy estimates.

References

Dalziel, S. B., Hughes, G. O., and Sutherland, B. R. (2000). Whole-field density measurements by 'synthetic schlieren'. *Experiments in Fluids*, 28(4):322–335.

Hill, D. F. (2002). General density gradients in general domains: the two-tank method revisited. *Experiments in Fluids*, 32(4).

King, B., Stone, M., Zhang, H. P., Gerkema, T., Marder, M., Scott, R. B., and Swinney, H. L. (2012). Buoyancy frequency profiles and internal semidiurnal tide turning depths in the oceans. *Journal of Geophysical Research: Oceans*, 117(C4).

Lighthill, J. (1974). *Waves in fluids*. Cambridge University Press.

Nappo, C. J. (2002). *An introduction to atmospheric gravity waves*. Academic Press, San Diego, California.

Paoletti, M. S., Drake, M., and Swinney, H. L. (2014). Internal tide generation in nonuniformly stratified deep oceans. *Journal of Geophysical Research: Oceans*, 119(3):1943–1956.

Pedlosky, J. (2003). *Waves in the Ocean and Atmosphere*. Springer-Verlag Berlin Heidelberg, Germany.

St. Laurent, L. C. and Garrett, C. (2002). The role of internal tides in mixing the deep ocean. *Journal of Physical Oceanography*, 32(10):2882 – 2899.

Sutherland, B. R. (2010). *Internal Gravity Waves*. Cambridge University Press, Cambridge, United Kingdom.

Wunsch, S. and Brandt, A. (2012). Laboratory experiments on internal wave interactions with a pycnocline. *Expts. in Fluids*, 53:1663–1679.